Revisiting the crystal structure of rhombohedral lead metaniobate

Gerhard Henning Olsen,[†] Magnus Helgerud Sørby,[‡] Bjørn Christian Hauback,[‡] Sverre Magnus Selbach,[†] and Tor Grande[*,†]

Norwegian University of Science and Technology (NTNU), Trondheim, Norway, and Institute for Energy Technology (IFE), Kjeller, Norway

---

[*]To whom correspondence should be addressed
[†]NTNU
[‡]IFE

Abstract

Lead metaniobate ($PbNb_2O_6$) can exist both as a stable rhombohedral and a metastable orthorhombic tungsten-bronze-type polymorph. While the orthorhombic is a well-known ferroelectric material, the rhombohedral polymorph has been far less studied. The crystal structure and energetic stability of the stable rhombohedral polymorph of lead metaniobate is re-examined by powder X-ray diffraction and powder neutron diffraction in combination with ab-initio calculations. We show that this structure is described by the polar space group $R3$, in contradiction to the previously reported space group $R3m$. The crystal structure is unusual, consisting of edge-sharing dimers of $NbO_{6/2}$ octahedra forming layers with six- and threefold rings of octahedra, and lead ions in channels formed by these rings. The layers are connected by corner-sharing between octahedra. Finally, the crystal structure is discussed in relation to other AB_2O_6 compounds with B = Nb, Ta.

Introduction

Lead metaniobate ($PbNb_2O_6$ or PN) is one of the simplest compounds to crystallize in the tungsten-bronze-type structure.[1] The tungsten-bronze polymorph is orthorhombic (denoted o-PN) and ferroelectric with a high Curie temperature of 570 °C.[2] The paraelectric tungsten-bronze has a tetragonal crystal structure (t-PN). A large anisotropy in electromechanical coupling factors and a very low mechanical quality factor makes the material suitable for high-temperature electroacoustic applications.[3] The t-PN polymorph is, however, metastable with respect to a rhombohedral polymorph (r-PN) below a transition temperature reported at 1200–1250 °C,[4–6] and this thermodynamically stable low-temperature phase has not been reported to have attractive properties. The phase transition between the t-PN and r-PN polymorphs is reconstructive and sluggish, so the metastable tungsten-bronze phase can be obtained by quenching the material from above the r-PN to t-PN transition at 1200–1250 °C.[4]

Numerous attempts have been done to stabilize the tungsten-bronze phase, e.g. by molten salt methods,[7,8] hydrothermal synthesis,[9] or formation of solid solutions.[10] The rhombohedral polymorph, on the other hand, has received comparatively little attention, although the possibility of attractive piezoelectric properties has been suggested also for this polymorph, with one work reporting a possible ferroelectric phase transition at 815 °C.[11] Still, investigations on the crystal structure and properties of the r-PN polymorph are few.[11–14] Here, we re-examine the crystal structure of r-PN by powder X-ray- and powder neutron diffraction combined with density functional theory calculations, with particular focus on determining the correct space group symmetry. We show that, contrary to previous assumptions,[12,13] $R3m$ is not the correct space group symmetry for r-PN. Based on experimental and computational data, we demonstrate that the structure is described by the space group $R3$ or the closely related space group $R\bar{3}$. We argue that $R3$ is the more plausible of the two, based on reported high-temperature properties of r-PN which indicate that the low-temperature space group symmetry is polar. The fact that the space

group is polar motivates further studies of possible piezoelectric properties.

Experimental work

Powders of lead metaniobate were prepared by conventional solid-state synthesis. PbO (Aldrich, 99.999%) and Nb_2O_5 (Aldrich, 99.99%) powders were mixed in equimolar amounts with a mortar and pestle, uniaxially pressed into 25 mm pellets and fired at 850 °C for 2 hours in a sealed alumina crucible. The pellets were crushed down, and pressing and firing was repeated twice, for a total of three 2-hour firings at 850 °C. The sample was finally crushed to a powder and annealed for 30 minutes at 550 °C prior to structural analysis in order to remove possible strain from the crushing.

Powder X-ray diffraction was performed at room temperature with a Siemens D5005 diffractometer in Bragg–Brentano geometry, with Cu $K\alpha_1$ radiation, a primary graphite monochromator and a Braun position sensitive detector. Data was collected in a 2θ range of 5°–110° with a step size of 0.015°.

Powder neutron diffraction data were collected with the PUS diffractometer at the JEEP II reactor at Institute for Energy Technology at Kjeller, Norway. Neutrons with a wavelength of 1.5555 Å were provided from a vertically focusing Ge monochromator using the (511) reflection and a take-off angle of 90°. Data were collected at room temperature in a 2θ range of 10°–130° in steps of 0.05° with two detector banks; each with 6 horizontally stacked ^{3}He-filled position sensitive detector tubes covering 20° in 2θ.[15]

Rietveld refinements were performed with both data sets simultaneously using the Bruker AXS Topas 4.2 software, with structural data from Mahé[13] used as starting point. The datasets were refined according to the symmetry constraints of five distinct rhombohedral space groups: $R\bar{3}m$ (166), $R3m$ (160), $R32$ (155), $R\bar{3}$ (148) and $R3$ (146). The rhombohedral setting was used for all the space groups, and Pb was anchored at $(0, 0, 0)$ for the Pb1 Wyckoff position for the polar space groups $R3m$ and $R3$ (see Table 1). The

background intensity was fitted to a Chebychev polynomial, and peak shapes were fitted to a Pearson type VII profile for X-ray data and a Thompson–Cox–Hastings pseudo-Voigt profile for neutron data. Lattice parameters and atomic positions were refined according to the atomic degrees of freedom described in Table 1, and isotropic thermal displacement factors were refined under the constraint that all atoms of the same element on the same Wyckoff site have the same displacement factors.

Table 1: Wyckoff sites and atomic positions for each of the five space groups considered in this work (the notation (x, x, x) means $x = y = z$). The bottom line gives the atomic degrees of freedom (DOF) for each space group, i.e., the total number of free variables in the atomic coordinates. For the polar groups $R3$ and $R3m$, the atomic DOF is one less than the number of free variables due to anchoring of Pb1 at $(0, 0, 0)$.

Atom	$R3$	$R\bar{3}$	$R32$	$R3m$	$R\bar{3}m$
Pb1	$1a$	$1a$	$1a$	$1a$	$1a$
	(x, x, x)	$(0, 0, 0)$	$(0, 0, 0)$	(x, x, x)	$(0, 0, 0)$
Pb2	$1a$	$2c$	$2c$	$1a$	$2c$
	(x, x, x)	(x, x, x)	(x, x, x)	(x, x, x)	(x, x, x)
Pb3	$1a$	—	—	$1a$	—
	(x, x, x)			(x, x, x)	
Nb1	$3b$	$6f$	$3e$	$6c$	$6g$
	(x, y, z)	(x, y, z)	$(1/2, y, -y)$	(x, y, z)	$(x, -x, 1/2)$
Nb2	$3b$	—	$3e$	—	—
	(x, y, z)		$(1/2, y, -y)$		
O1	$3b$	$6f$	$3d$	$6c$	$6f$
	(x, y, z)	(x, y, z)	$(0, y, -y)$	(x, y, z)	$(x, -x, 0)$
O2	$3b$	$6f$	$3d$	$3b$	$6h$
	(x, y, z)	(x, y, z)	$(0, y, -y)$	(x, x, z)	(x, x, z)
O3	$3b$	$6f$	$6f$	$3b$	$6h$
	(x, y, z)	(x, y, z)	(x, y, z)	(x, x, z)	(x, x, z)
O4	$3b$	—	$6f$	$3b$	—
	(x, y, z)		(x, y, z)	(x, x, z)	
O5	$3b$	—	—	$3b$	—
	(x, y, z)			(x, x, z)	
O6	$3b$	—	—	—	—
	(x, y, z)				
Atomic DOF	26	13	11	16	7

Computational details

Density functional theory (DFT) calculations were done with the VASP code.[16–19] Calculations of the exchange-correlation energy were done both within the local density approximation (LDA), and within the generalized gradient approximation (GGA) with the functionals PBE[20] and PBEsol.[21] Projector-augmented wave potentials[22,23] were used, treating 14 valence electrons for Pb ($5d^{10}6s^26p^2$), 13 for Nb ($4s^24p^64d^35s^2$) and 6 for O ($2s^22p^4$). Well-converged results were achieved when wave functions were expanded in a plane wave basis set up to an energy cutoff of 550 eV, and Brillouin zone integration was performed on a $2 \times 2 \times 2$ Monkhorst–Pack grid.[24] For geometry optimization, lattice vectors and atomic coordinates were relaxed until the forces on the ions were less than 1×10^{-4} eV Å^{-1}.

The experimental structures, as obtained by refinement of diffraction data, were relaxed using the three functionals described above. Three different contraints were applied: (a) Ionic relaxation at the experimental lattice parameters; (b) relaxation of ions and lattice vectors with the constraint that the unit cell volume be constant and equal to the experimental volume; (c) full relaxation of both ions and lattice vectors with no constraints on the unit cell volume (see Figure 2). The total energies were then compared between cells of different space group symmetries.

Lattice dynamical calculations were performed with the force constant method,[25] using VASP for calculation of Hellmann–Feynman forces and the Phonopy code for calculation of the approximate dynamical matrix and the full phonon dispersion. A $2 \times 2 \times 2$ supercell was used, and symmetry-inequivalent atoms displaced by 0.01 Å in each direction (see Supporting information for details).

Results

Diffraction experiments

The five space groups considered ($R3$, $R\bar{3}$, $R32$, $R3m$ and $R\bar{3}m$) have the same selection rules for diffraction, so the distinction between the different candidate space groups relies only on the intensities of the Bragg reflections.

X-ray and neutron diffractograms are shown in Figure 1 together with Rietveld refinements within space group $R3$, which gave the best fit both for the two datasets separately and for simultaneous refinement (individual refinements and relevant parameters are given in Supporting information). The goodness of fit for the different space groups is summarized in Table 2 together with lattice parameters from the refinements. Space group $R\bar{3}m$ yielded the worst fit, and gave rise to a systematic deviation for certain reflections between experimental data and the fit. Also the previously reported[12] space group $R3m$ gave systematic deviations for certain reflections, and a magnification of the representative (321) reflection is shown in the insets of Figure 1, comparing the fit for space group $R3m$ and $R3$. Similar deviations of comparable magnitude are apparent also in other reflections throughout the Q range, notably the $(1\bar{4}\bar{3})$ and $(03\bar{7})$ reflections at approximately $Q = 4.55\,\text{Å}^{-1}$ and $Q = 6.52\,\text{Å}^{-1}$, respectively (see Supporting information). For space group $R3$, which gave the best fit, both the experimental (joint refinement of X-ray and neutron diffraction data) and the optimized atomic coordinates are given in Table 3.

For all space groups, the refined structures show distinct differences from the previously reported structures, refined in space group $R3m$.[13,14] The most pronounced difference is that the $NbO_{6/2}$ octahedra are far less deformed, with less variation in the Nb–O bond lengths. This will be further discussed below.
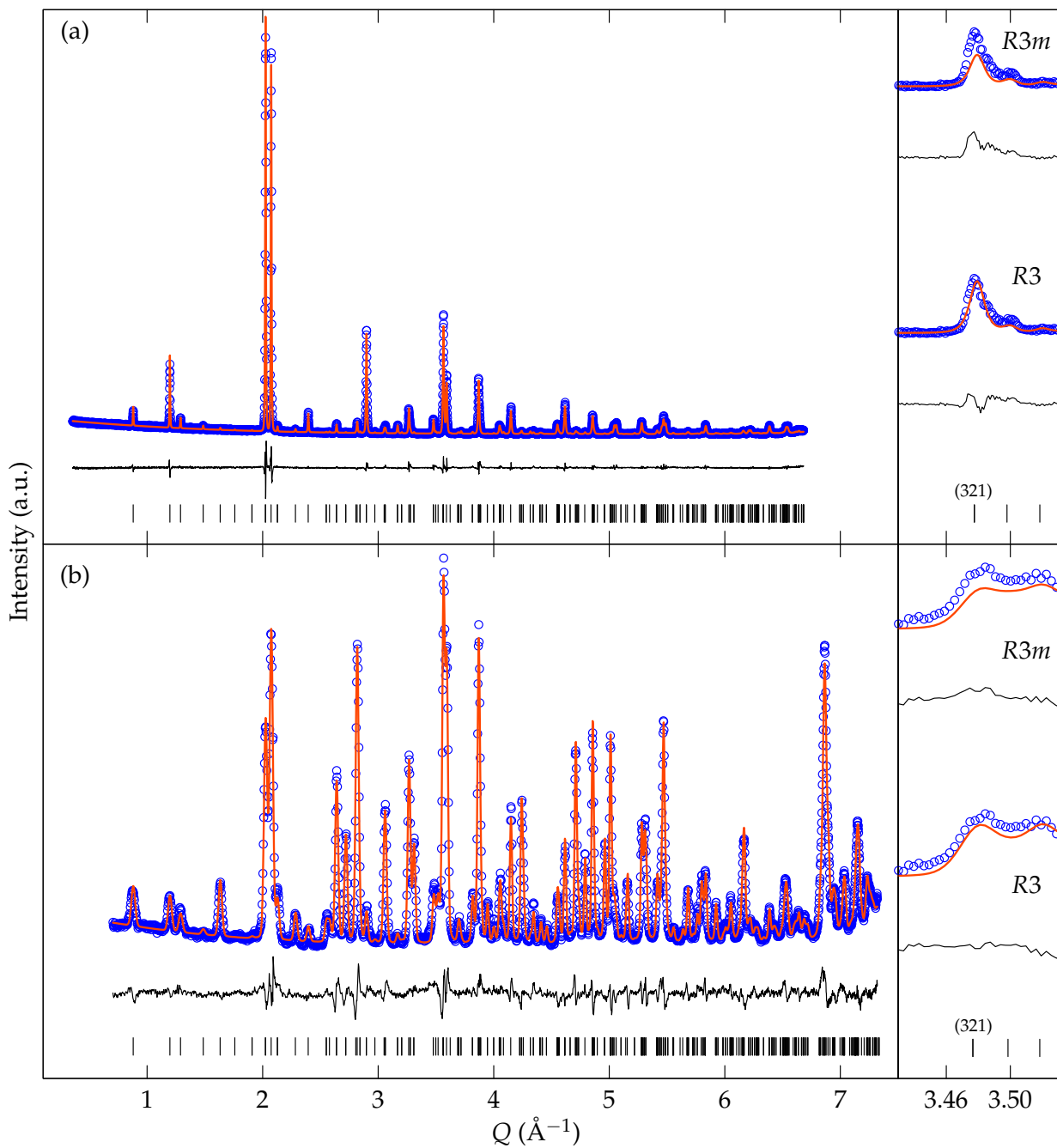
Figure 1: (a) Powder X-ray and (b) powder neutron diffractograms, showing observed (blue circles) and calculated (red line) intensity for space group $R3$, and their difference (black line) as a function of the scattering vector ($Q = 2\pi/d$). Black tick marks show the position of individual Bragg reflections. Zoom-in to the right shows a comparison between refinements within space groups $R3$ and $R3m$.

Table 2: Lattice parameters at room temperature, and quality of fit for joint refinement of X-ray and neutron data within each of the five space groups considered (estimated standard deviations in parenthesis). Literature values for $R3m$ (converted from hexagonal setting) are included at the bottom.

Space group	Lattice parameters		Quality of fit		
	a (Å)	α (°)	$R_p(\%)$	$R_{wp}(\%)$	χ^2
$R3$	7.17530(7)	93.9548(5)	6.62	9.05	1.89
$R\bar{3}$	7.17530(7)	93.9552(5)	6.85	9.29	1.94
$R32$	7.17508(9)	93.9566(6)	8.21	11.66	2.44
$R3m$	7.17521(8)	93.9555(6)	7.65	10.69	2.23
$R\bar{3}m$	7.17516(10)	93.9564(6)	8.51	11.93	2.49
$R3m$[12]	7.183	93.94			
$R3m$[14]	7.1654	93.908			

Computational results

Additional information on the relative stability of the different space groups is obtained from the calculated energies of the candidate structures. The energies of the possible structures are shown in Figure 2(a)–(c), corresponding to the three different relaxation constraints described above. For full relaxation with no volume constraints, the volume after relaxation is shown in Figure 2(d). All energies are reported per formula unit of $PbNb_2O_6$, and given relative to the structure with the lowest symmetry, $R3$. The energy of the $R32$ structure is omitted from the figures, since this experimental structure relaxes into the higher-symmetry space group $R\bar{3}m$. Because of this apparent instability, and the relatively poor goodness of fit for Rietveld refinement within this space group (Table 2), $R32$ was not considered further as a plausible space group symmetry for r-PN at ambient temperature.

For the three space groups $R\bar{3}m$, $R3m$ and $R3$, the calculated energies correlate with the degree of symmetry, with $R\bar{3}m$ having the highest symmetry and the highest calculated energy, $R3m$ intermediate, and $R3$ the lowest. $R\bar{3}$, however, does not follow this trend: It has essentially the same energy as $R3$, while at the same time possessing a higher symmetry and merely half as many atomic degrees of freedom as $R3$ (Table 3). This result is the

9

same for all the relaxation methods used. Lattice dynamical calculations similarly show negligible difference between the dynamical stability of the $R\bar{3}$ and $R3$ structures, while the $R3m$ and $R\bar{3}m$ structures have instabilities which correlate with their higher energy (phonon dispersions are included in Supporting information).

Atomic positions for the $R3$ structure, both experimental (joint refinement) and after computational optimization (full relaxation with the PBEsol functional), are given in in Table 3.

Table 3: Atomic positions and unit cell parameters ($R3$, rhombohedral setting) based on joint refinement of diffraction data, and after geometry optimization by DFT calculations (PBEsol, unconstrained relaxation). B_{eq} is the isotropic thermal displacement factors, constrained to be the same for all atoms of the same element. Optimized atomic positions from DFT calculations are reported with a numerical precision corresponding to the uncertainty in the experimental data.

| Atom	Experimental				Optimized		
	x	y	z	B_{eq} (Å^2)	x	y	z
Pb1	0	0	0	1.48(3)	0	0	0
Pb2	0.3527(4)	0.3527(4)	0.3527(4)	1.48(3)	0.3527	0.3527	0.3527
Pb3	0.6889(5)	0.6889(5)	0.6889(5)	1.48(3)	0.6764	0.6764	0.6764
Nb1	0.5338(11)	0.2006(9)	0.8384(10)	0.06(3)	0.5403	0.1965	0.8405
Nb2	0.1531(10)	0.5117(8)	0.8068(9)	0.06(3)	0.1562	0.5122	0.8123
O1	0.404(2)	0.947(2)	0.678(2)	0.40(3)	0.403	0.959	0.678
O2	0.9617(14)	0.3878(14)	0.668(2)	0.40(3)	0.9501	0.3941	0.675
O3	0.760(2)	0.773(2)	0.065(2)	0.40(3)	0.772	0.772	0.058
O4	0.055(2)	0.053(2)	0.5216(14)	0.40(3)	0.058	0.058	0.5129
O5	0.571(2)	0.580(2)	0.293(2)	0.40(3)	0.581	0.581	0.294
O6	0.292(2)	0.294(2)	0.8515(12)	0.40(3)	0.295	0.295	0.8398
a (Å)	7.17530(7)				7.15572		
α (°)	93.9548(5)				94.0297		
V_{cell} (Å^3)	366.652(11)				363.551		
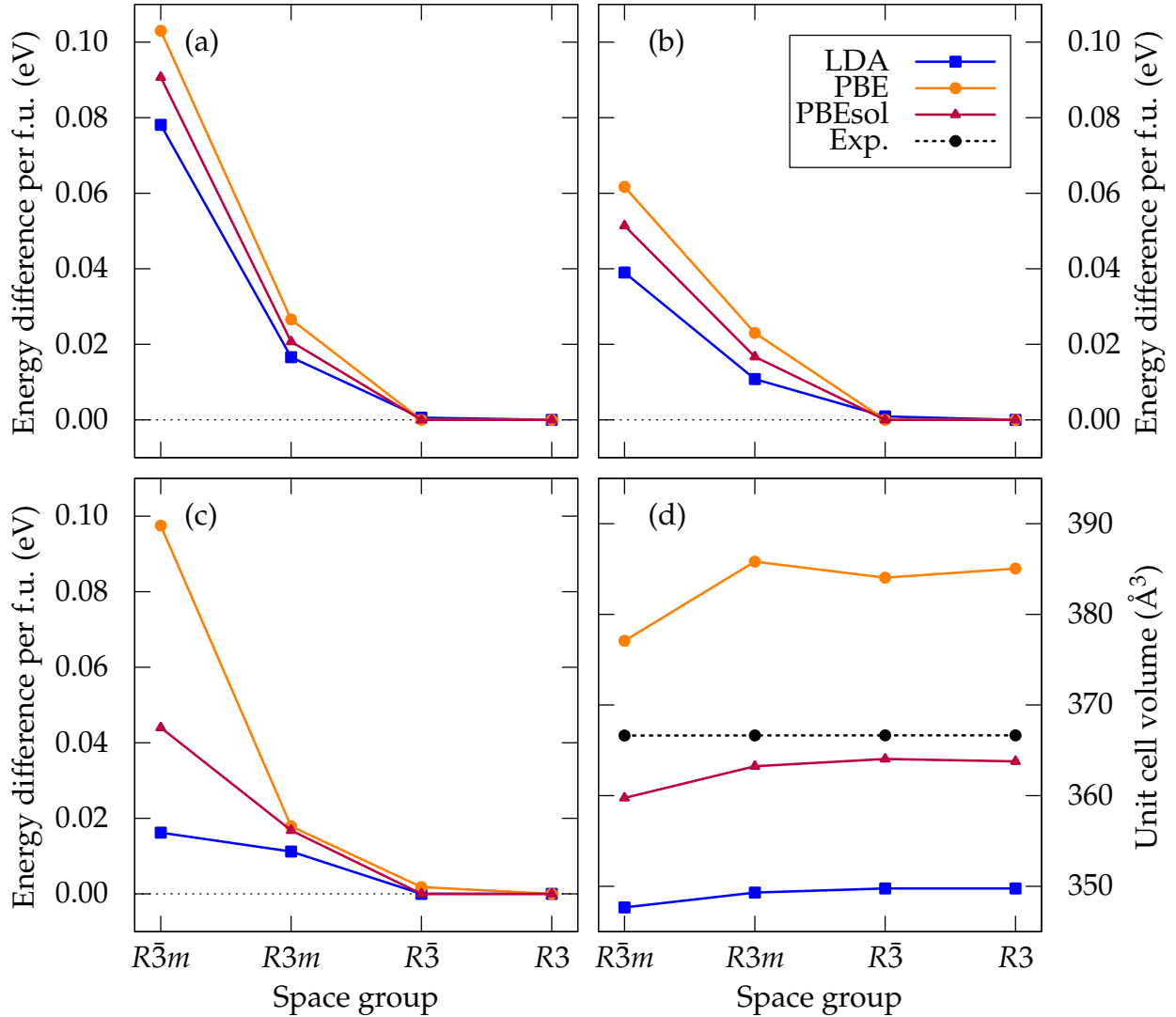
Figure 2: Calculated energy per formula unit for each of the space groups considered, after (a) ionic relaxation at experimental lattice parameters; (b) relaxation of ions and lattice vectors at constant experimental volume; (c) unconstrained relaxation of ions and lattice vectors. Energies are given relative to the lowest-energy space group $R3$. (d) Unit cell volume after unconstrained relaxation with the three functionals, including the experimental volume.

Discussion

Determination of space group symmetry

Both refinement of the diffraction data, and comparison of DFT energies, point to either of $R\bar{3}$ or $R3$ as the most likely space group symmetries for r-PN at ambient conditions. This is in contrast to earlier works,[12,13] which conclude that the space group is $R3m$. Figure 3 gives the group–subgroup relations between all five space groups considered in this work. The path involving space group $R32$ can be excluded based on the poor Rietveld fit (Table 2) and the instability with respect to force-based geometry optimization.

The difference in quality of fit is quite small between $R3$ and $R\bar{3}$, as is evident from Table 2. A reasonable way of testing the significance of this difference is by Hamilton's R-ratio test,[26] which is based on the well-known F-test. In our case, the ratio of R_{wp} factors for the $R\bar{3}$ and $R3$ refinements is $\mathcal{R} = 1.027$. For the joint refinement, the total number of (hkl) reflections is 730, with 60 parameters refined for $R3$ and 47 for $R\bar{3}$ (the difference of 13 corresponding to the difference in atomic degrees of freedom, as given in Table 1). From Hamilton's table,[26] we read off $\mathcal{R}_{13,670,0.005} = 1.023$, meaning that the probability of $R3$ actually being a better model than $R\bar{3}$ for this refinement, is higher than 0.995. The same result is obtained if the X-ray and neutron diffraction data is refined and tested individually, so we conclude that $R3$ is a significantly better model than $R\bar{3}$.

In addition to the rhombohedral space group symmetries shown in Figure 3, one could in principle also consider refinements within further subgroups of $R3$ and $R\bar{3}$, i.e., the trigonal groups $P3$ (143), $P3_1$ (144), $P3_2$ (145) and $P\bar{3}$ (147). $P3_1$ and $P3_2$, however, can be excluded, as the 3-fold screw axes are not compatible with the stacking pattern found in this structure (further described below). $P3$ and $P\bar{3}$, although possible from a structural point of view, do not yield a better fit than $R3$, despite a higher number of refined parameters for the trigonal groups. Because of this, we see no reason not to keep the rhombohedral lattice centering, restricting the possible space groups to those shown in

Figure 3.

A general observation for all energy calculations, is that $R\bar{3}m$ has the highest energy, $R3m$ intermediate, and $R\bar{3}$ and $R3$ are essentially at the same, lowest energy. This is true for all methods of geometry optimization, and for all functionals, as shown in Figures 2(a)–(c). In practice, the experimental $R3$ structure relaxes towards $R\bar{3}$ symmetry, and the distinction between them is ultimately a matter of tolerance during the symmetry analysis.[27] For the constrained relaxations (Figure 2(a)–(b)), the $R3$ structure is regarded as having $R\bar{3}$ symmetry for tolerances higher than $3 \cdot 10^{-4}$ if relaxed with PBE, and $3 \cdot 10^{-2}$ if relaxed with PBEsol. For the unconstrained relaxation (Figure 2(c)), the threshold values are $5 \cdot 10^{-4}$ for LDA and $1 \cdot 10^{-3}$ for PBEsol. In other words, the structures relaxed using PBEsol give the largest structural differences between $R3$ and $R\bar{3}$, although the two space groups are hard to distinguish in all cases.

The graphs in Figure 2 confirm certain well-known properties of the functionals used.[28] LDA has an inherent tendency to overbind, which is reflected in a relaxed cell volume which is smaller than the experimental volume by around 5%, as seen in Figure 2(d). The PBE functional, on the other hand, slightly overcorrects this deviation, producing a unit cell volume which is around 5% larger than the experimental value. The PBEsol functional is intended to improve on PBE for equilibrium properties of solids such as bond lengths and lattice parameters, and the volume calculated with PBEsol comes very close to the experimental volume. This difference between the functionals is also reflected in the energies for the different space groups. As spontaneous polarization in solids requires a certain volume for the displacement of ions, the underbinding PBE functional is expected to favor polar space groups more than the overbinding LDA. For all calculations, PBE gives the largest energy difference between the polar $R3$ and the non-polar $R\bar{3}m$, and LDA the smallest. The effect of this is most pronounced for the unconstrained relaxations as shown in Figure 2(c).

While the diffraction data is convincing, $R3$ and $R\bar{3}$ are still so similar in structure

and energy that care must be taken to properly distinguish between them. The difference between the space group symmetries $R3$ and $R\bar{3}$ is the presence of an inversion center in the latter, making the space group non-polar. This is obviously important for applications of the material, as e.g., pyro- and ferroelectricity requires a polar space group. Lopatin[11] suggested that a rhombohedral $R3m$ polymorph might transform to the non-polar space group $R\bar{3}m$ at high temperatures, based on an observed contraction of the polar axis (hexagonal $[001]$ direction, rhombohedral $[111]$ direction) upon heating to $815\,^\circ$C, followed by normal thermal expansion. Such an anisotropic thermal expansion would be expected to accompany the transition from a polar to a non-polar space group, e.g., from $R3m$ to $R\bar{3}m$ or from $R3$ to $R\bar{3}$, while a transition between two polar (or two non-polar) space groups is likely to be much more subtle. To explain the anisotropic thermal expansion reported by Lopatin,[11] it is therefore required that the ambient-temperature space group be polar. This, in addition to the statistical significance of the R_{wp} factors from the refinement, makes $R3$ the most probable space group symmetry.
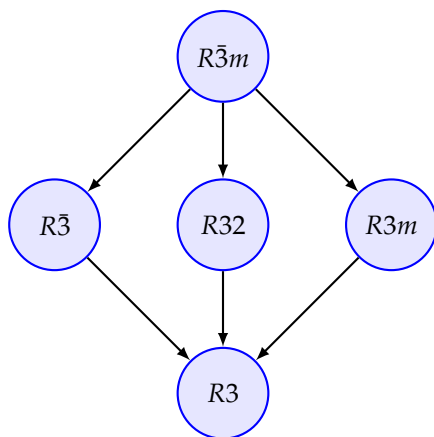

Figure 3: Group–subgroup relations between the space group symmetries considered in this study.

Description of the crystal structure

The main characteristic features of the crystal structure of r-PN are illustrated in Figure 4. Rhombohedral lead metaniobate is not a "layered" structure in the usual sense, although it

is natural to picture it as being built from layers due to the anisotropy in crystal structure, polyhedral connectivity and bonding. The fundamental building blocks are *dimer* units, made up of two edge-sharing $NbO_{6/2}$ octahedra as shown in Figure 4(a). The dimers are corner-linked, creating layers or sheets as shown in Figure 4(b). The layers have a point group symmetry which is nearly hexagonal, although, as will be further discussed below, the point group symmetry of the crystal is trigonal due to the stacking sequence and the polyhedral connectivity between layers.

Three different kinds of rings of corner- and edge-sharing octahedra can be identified in the layers: One hexagonal, and two triangular rings that are symmetrically inequivalent. In Figure 4(b), the hexagonal ring (yellow) is in the middle, surrounded by six triangular rings (red and blue). Each of the triangular rings is pointing either up (red) or down (blue) within the plane of the figure, thereby distinguishing the two types. In a single layer of ideal hexagonal symmetry ($P6/mmm$), the two triangular rings would be equivalent.

The layers are stacked as shown in Figure 4(c), with a repeating sequence of three layers. The rings in each layer form channels parallel to the hexagonal c axis. Lead cations are positioned inside these channels, between the layers. In the three-dimensional structure, every hexagonal ring has a triangular ring both above and below. This stacking sequence, with mixing of hexagonal and triangular rings, lowers the symmetry of the crystal from the ideal 6-fold, to the 3-fold symmetry observed. It can be noted that each of the three rings is associated with one of the three Wyckoff positions for lead in space group $R3$ (Table 1).

In addition to the stacking sequence, the polyhedral connectivity itself introduces tilts and distortions that prevent the ideal hexagonal symmetry from being realized. Between the layers, only corner-sharing connects the $NbO_{6/2}$ octahedra, whereas both corners and edges are shared within the layers. It is not possible to connect the layers as shown in Figure 4(c) without introducing symmetry-breaking distortions of the octahedra.

The octahedral deformation in the crystal structure reported here, is much less than reported in the previous work by Mahé.[13] He pointed out the large variation in Nb–O bond

lengths, but remarked that this variation was not significant considering the experimental uncertainty in the oxygen positions. The uncertainty in oxygen positions in Mahé's work[13] was on the order of $0.1\,\text{Å}$, while here it is an order of magnitude less (Table 3), as a consequence of the neutron scattering cross section of oxygen being comparable to those of lead and niobium.

Structures built from $BO_{6/2}$ dimer units are well known for niobates and tantalates of AB_2O_6 stoichiometry, with A = Ca, Sr or Ba.[29] In particular, the hexagonal high-temperature form of $BaTa_2O_6$[30] bears a resemblance to the layer-like structure of r-PN described here, with a combination of dimers and corner-sharing octahedra. The hexagonal $BaTa_2O_6$ structure is arguably even more complex than r-PN, containing both three-, five- and six-membered rings. Half of the $TaO_{6/2}$ octahedra in hexagonal $BaTa_2O_6$ share only corners with other octahedra, while in the r-PN structure, every $NbO_{6/2}$ octahedron is part of a dimer.

The particular crystal structure found in r-PN is not commonly encountered, and is rather unique. It was not reported to exist for other compounds in a recent review[31] of AB_2O_6 compounds, although $PbRe_2O_6$ has previously been reported[32] as isotypic with r-PN, with space group $R\bar{3}m$. $PbTa_2O_6$ has also been reported[33] to exist in a non-ferroelectric rhombohedral form, analogous to r-PN, but no detailed structural study of this compund has to our knowledge been performed.

The presence of a polar space group symmetry in r-PN is interesting, since it is a requirement for pyro- and ferroelectricity. It thereby opens up for possible device applications, such as in piezoelectric sensors.

Conclusion

The ambient-temperature phase of lead metaniobate has been investigated by powder X-ray diffraction and powder neutron diffraction in combination with ab-initio DFT calcu-
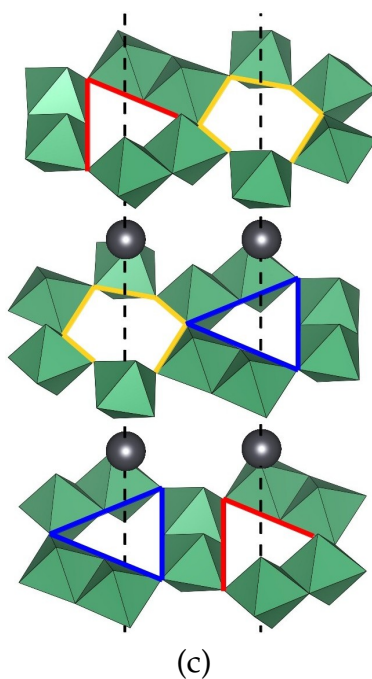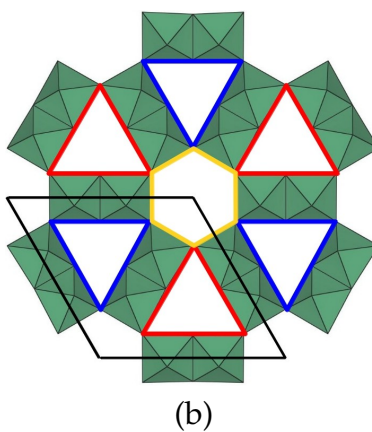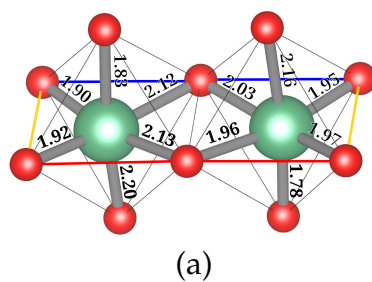
(a)

(b)

(c)

Figure 4: Layered structure of PN: (a) Single dimer consisting of two edge-sharing $NbO_{6/2}$ octahedra. Experimental Nb–O bond lengths for space group $R3$ given in Å; edges colored as in (b) and (c). (b) Single layer showing the hexagonal rings (yellow) and the two types of triangular rings (red and blue). Black line marks one hexagonal unit cell. (c) Stacking sequence of layers. The layers are stretched apart along the hexagonal (001) axis for clarity. Lead ions (grey spheres) are situated inside channels formed by openings in the layers. Figure created with VESTA.[34]

lations. It is found that the space group symmetry of r-PN is most likely the polar group *R*3, in contrast to previous assumptions of *R*3*m* being the correct space group for this structure. Furthermore, the new data on atomic positions in r-PN shows a structure with significantly less deformation of the $NbO_{6/2}$ octahedra than in previous works. Rhombohedral lead metaniobate has a highly anisotropic structure, and is conveniently described as being built from layers. Within the layers, $NbO_{6/2}$ octahedra share edges to form dimers, which are connected by corner-sharing, at the same time forming triangular and hexagonal rings in the layers. The layers are connected by corner-sharing, with the rings in each layer forming channels that accomodate the lead cations.

Acknowledgement

Supporting Information Available

Rietveld refinements of powder diffraction data within different space groups, as well as X-ray and neutron diffraction data refined separately. Lattice parameters from geometry optimization by DFT are also given, along with full phonon dispersions for the space group symmetries considered. This material is available free of charge via the Internet at `http://pubs.acs.org/`.

Author information

Corresponding author

*E-mail: tor.grande@ntnu.no

References

(1) Lines, M. E.; Glass, A. M. *Principles and applications of ferroelectrics and related materials*; Clarendon Press; Oxford University Press, 2001

(2) Goodman, G. *J. Am. Ceram. Soc.* **1953**, *36*, 368–372

(3) Gallego-Juárez, J. A. *J. Phys. E: Sci. Instrum.* **1989**, *22*, 804–816

(4) Francombe, M. H. *Acta Cryst.* **1956**, *9*, 683–684

(5) Rivolier, J.-L.; Ferriol, M.; Cohen-Adad, M.-T. *Eur. J. Solid State Inorg. Chem.* **1995**, *32*, 251–262

(6) Lee, H. S.; Kimura, T. *J. Am. Ceram. Soc.* **1998**, *81*, 3228–3236

(7) Kimura, T.; Machida, M.; Yamaguchi, T.; Newnham, R. E. *J. Am. Ceram. Soc.* **1983**, *66*, c195–c197

(8) Li, C. C.; Chiu, C. C.; Desu, S. B. *J. Am. Ceram. Soc.* **1991**, *74*, 42–47

(9) Lu, C.-H.; Chyi, N. *Mater. Lett.* **1996**, *29*, 101–105

(10) Sahini, M. G.; Grande, T.; Fraygola, B.; Biancoli, A.; Damjanovic, D.; Setter, N. *J. Am. Ceram. Soc.* **2014**, *97*, 220–227

(11) Lopatin, S. S.; Medvedev, E. S.; Raevskii, I. P. *Zh. Neorg. Khim.* **1985**, *30*, 2102–2106

(12) Mahé, R. *Bull. Soc. Chim. Fr.* **1966**, 3401–3403

(13) Mahé, R. *Bull. Soc. Chim. Fr.* **1967**, 1879–1884

(14) Chakraborty, K. R.; Sahu, K. R.; De, A.; De, U. *Integr. Ferroelectr.* **2010**, *120*, 102–113

(15) Hauback, B. C.; Fjellvåg, H.; Steinsvoll, O.; Johansson, K.; Buset, O. T.; Jørgensen, J. *J. Neutron Research* **2000**, *8*, 215–232

(16) Kresse, G.; Hafner, J. *Phys. Rev. B* **1993**, *47*, 558–561

(17) Kresse, G.; Hafner, J. *Phys. Rev. B* **1994**, *49*, 14251–14269

(18) Kresse, G.; Furthmüller, J. *Comput. Mater. Sci.* **1996**, *6*, 15–50

(19) Kresse, G.; Furthmüller, J. *Phys. Rev. B* **1996**, *54*, 11169–11186

(20) Perdew, J. P.; Burke, K.; Ernzerhof, M. *Phys. Rev. Lett.* **1996**, *77*, 3865–3868

(21) Perdew, J. P.; Ruzsinszky, A.; Csonka, G. I.; Vydrov, O. A.; Scuseria, G. E.; Constantin, L. A.; Zhou, X.; Burke, K. *Phys. Rev. Lett.* **2008**, *100*, 136406–136406

(22) Blöchl, P. E. *Phys. Rev. B* **1994**, *50*, 17953–17979

(23) Kresse, G.; Joubert, D. *Phys. Rev. B* **1999**, *59*, 11–19

(24) Monkhorst, H. J.; Pack, J. D. *Phys. Rev. B* **1976**, *13*, 5188–5192

(25) Togo, A.; Oba, F.; Tanaka, I. *Phys. Rev. B* **2008**, *78*, 134106–134106

(26) Hamilton, W. C. *Acta Cryst.* **1965**, *18*, 502–510

(27) Stokes, H. T.; Hatch, D. M. *J. Appl. Crystallogr.* **2005**, *38*, 237–238

(28) Hafner, J. *J. Comput. Chem.* **2008**, *29*, 2044–2078

(29) Galasso, F.; Layden, G.; Ganung, G. *Mater. Res. Bull.* **1968**, *3*, 397–408

(30) Layden, G. K. *Mater. Res. Bull.* **1968**, *3*, 349–360

(31) Beck, H. P. *Z. Kristallogr.* **2013**, *228*, 271–288

(32) Wentzell, I.; Fuess, H.; Bats, J. W.; Cheetham, A. K. *Z. Anorg. Allg. Chem.* **1985**, *528*, 48–54

(33) Subbarao, E. C.; Shirane, G.; Jona, F. *Acta Cryst.* **1960**, *13*, 226–231

(34) Momma, K.; Izumi, F. *J. Appl. Crystallogr.* **2011**, *44*, 1272–1276

For Table of Contents Only

Diffraction experiments and DFT calculations are combined to give new insight about the crystal structure of rhombohedral lead metaniobate.